

Normal conducting superbend in an ultralow emittance storage ringF. Saeidi,^{1,*} R. Pourimani,¹ J. Rahighi,² H. Ghasem,^{2,3} and M. Laméhi Rachtí²¹*Department of Physics, Faculty of Science, Arak University, P.O. Box 8349-8-38156, Arak, Iran*²*Iranian Light Source Facility (ILSF), Institute for Research in Fundamental Sciences (IPM), P.O. Box 19395-5746, Tehran, Iran*³*School of Particles and Accelerators, Institute for Research in Fundamental Sciences (IPM), P.O. Box 19395-5531, Tehran, Iran*

(Received 19 May 2015; published 31 August 2015)

The Iranian Light Source Facility (ILSF) is a new 3 GeV synchrotron radiation laboratory in the Middle East. As the main radiation source, the ILSF storage ring is based on a five-bend achromat lattice providing an ultralow horizontal beam emittance of 0.48 nm rad. In order to produce very bright high energy radiation from the bending magnet, a superbend electromagnet is designed to replace the central low-field dipole of the bare lattice. In this paper, we present some design features of the ILSF storage ring bending magnet radiation source and discuss the detailed physical and mechanical design of the normal conducting superbend electromagnet. The related beam dynamics issues have been investigated as well.

DOI: 10.1103/PhysRevSTAB.18.082401

PACS numbers: 41.60.Ap, 41.85.Lc, 29.20.db, 29.27.-a

I. INTRODUCTION

The Iranian Light Source Facility (ILSF) project is the first Iranian synchrotron light laboratory which is in the design stage and will be built in the city of Qazvin located 150 km west of Tehran. It is conceived as a national synchrotron light source to provide a powerful source of x rays. It will cover the requirements of researchers in various scientific disciplines and will provide a major impetus for the multidisciplinary sciences. At the end of 2009, the Institute for Research in Fundamental Sciences (IPM) was selected as the executor to construct the facility [1–2].

The horizon of the ultralow beam emittance storage rings is based on the multibend achromat lattice structure, which improves the brightness 2–3 orders of magnitude higher than present synchrotron radiation sources [3–8]. The figure of merit of the ILSF storage ring follows the design trend of the modern synchrotron light sources. The designed ILSF storage ring lattice is based on the five-bend achromat (5BA) lattice. It is composed of 20 superperiods and provides 20 straight sections. One of them will be occupied with the injection equipment, and two of them are reserved for the rf cavities; the remaining straight sections are considered for installation of the insertion devices (IDs). Furthermore, the storage ring will serve up in total 20 beam lines from the central dipole magnets of the storage ring lattice. The ILSF storage ring circumference is 528 m, and the emittance of the electron beam would be

0.48 nm rad. Further information about the storage ring can be found in Ref. [9].

There are five pure dipoles in each superperiod and a total of 100 in the whole ring. Each dipole has a magnetic field of 0.75 T, length of 0.84 m, and deflection angle of 3.60°. The weak dipoles include no field gradient, having the advantages of lower fabrication cost with home industries and easier alignment in the ring. The radiated beam critical energy from such a dipole is limited to 4.48 keV at 3 GeV. This photon beam energy would be useful for several experiments in the soft x-ray regions, but it is low for the hard x-ray experiments. For the ILSF, the superbend solution would be superior to additional wigglers. In principle, a wiggler or wavelength shifter can be used in the storage ring to generate the required hard x rays, but there are many advantages to the superbend solution. The superbend can be employed instead of the ILSF bare lattice central bending magnet to be a source of bright high energy radiation without using up any straight sections. The lack of straight sections is a significant issue in the ILSF machine, since there will be totally 17 free straight sections for IDs. The superbends provide high capacity, serving up to 20 beam lines in the ILSF storage ring, while their fabrication cost is much lower than the IDs. Because of the smaller electron beam spot size, the superbends make available higher flux density than a wiggler, which is desirable from a scientific point of view. The total radiation power of the superbend beam line is significantly smaller than the wiggler beam line, which results to save energy [10]. Furthermore, the longitudinal field gradient provided by the superbend helps beam emittance reduction [11–14]. Therefore, the superbend magnet is chosen for use instead of the ILSF lattice central low-field dipole. This replacement is displayed in Fig. 1. It shows a superperiod of the ILSF storage ring where the lattice central dipole is replaced with a superbend magnet.

*Corresponding author.
farhad.saeidi@ipm.ir, saeidi.farhad@gmail.com

Published by the American Physical Society under the terms of the *Creative Commons Attribution 3.0 License*. Further distribution of this work must maintain attribution to the author(s) and the published article's title, journal citation, and DOI.

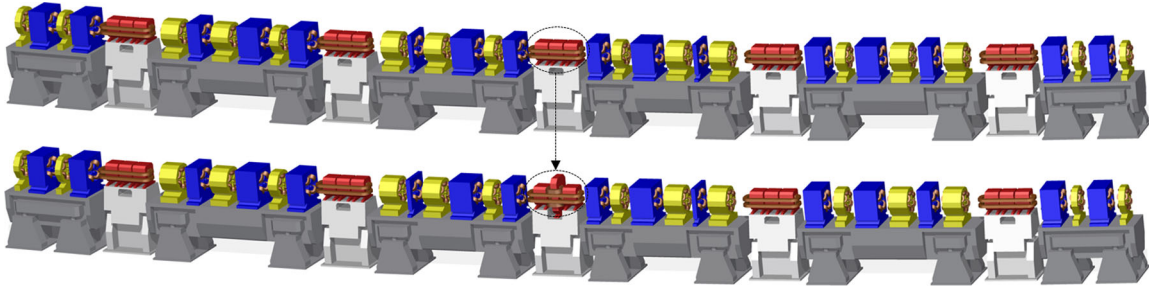


FIG. 1. The central low-field dipole in a period of the ILSF storage ring is replaced with a superbend magnet [15].

To simplify the magnet design, avoid a curved orbit dipole, and provide an easy fabrication procedure of this dipole for our local industries, each dipole in the bare lattice is divided in three straight dipole sections; see Fig. 1. All the sections have the same length of 28 cm and deflection angle of 1.2° . The middle section of the central low-field dipole is replaced with a thin high-field section.

There are three approaches of permanent, superconducting, and normal conducting magnets for design of the superbend. Because of the unchangeable field, remnant field sensitivity with the temperature, and aging effect of the permanent magnets [16] and because of the required advanced technologies of the superconducting approach, which is not necessary for a steering field less than 2 T [17], the ILSF superbend has been designed based on a normal conducting electromagnet. The valuable experiences in fabrication of electromagnets with home industries motivated us for this selection. Furthermore, the electromagnet superbend core material is locally available, while the permanent material must be procured from abroad, which makes the cost more expensive. The experiences of R&D fabricated magnet prototypes with home industries demonstrated that the laminated low carbon steel ST14 which is

locally available can be employed as the main material for fabrication of the superbend magnet [18–19]. It can provide a magnetic field of 1.4 T, which corresponds to the critical radiated beam energy of 8.38 keV desired for the users. With the use of such a superbend, the required high energy bright radiation would be available from the inserted high-field section, whose core length is 14.91 cm. The brilliance curves of the emitted radiation from the central low-field dipole and the mentioned superbend magnet are shown in Fig. 2. It indicates that the brilliance of the emitted photon beam from the superbend at its critical energy is almost 2–3 times higher than the case of a central low-field dipole.

This paper starts with the beam dynamics issues related to the use of the superbend magnet instead of the central dipole in the bare lattice. Impacts of the superbend on the ILSF beam parameters and the particle dynamics are discussed. The physical design of the normal conducting superbend including electrical and cooling calculations in two and three dimensions (2D and 3D) will be given next. The magnetic field quality, harmonic and statistical analyses, and end pole chamfering process are included. The related mechanical issues are described at the end. It should be noted that the FEMM [20], POISSON [21], MERMAID [22], and RADIA [23] software programs are used for the magnet design. The OPA [24] and ELEGANT [25] codes are employed for the beam dynamics studies. The SPECTRA [26] code is also utilized to study radiation properties. The subscripts x , y , and s in the paper indicate horizontal, vertical, and longitudinal directions, respectively.

II. BEAM DYNAMICS

A substantially lower emittance can be reached in a storage ring if the homogeneous bending magnets are replaced by devices of the same length with a varying longitudinal field. Furthermore, the local field enhancement will shift the critical energy towards higher values and satisfy the requirements of the hard x-ray user community [11–14]. These features were the main motivations for the ILSF to employ such step function dipoles (superbends) as the very interesting components for the compact high brightness light sources [10,27–29].

The natural emittance for the ring based on the 5BA lattice structure in the presence of the superbend is given by

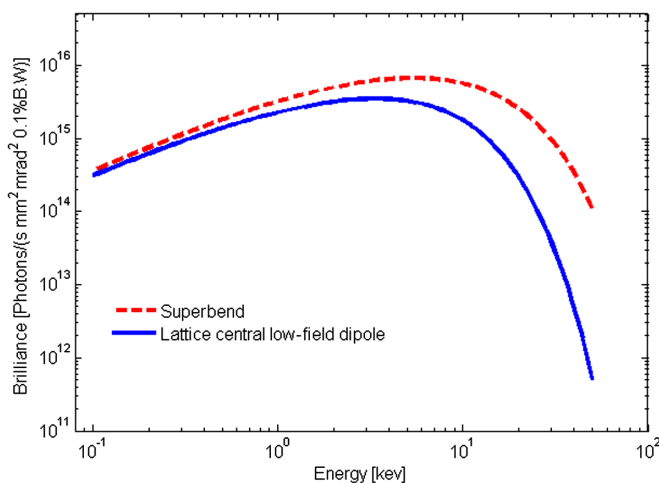


FIG. 2. On-axis brilliance of the emitted synchrotron radiation from the lattice central low-field dipole and the superbend magnet. The storage ring electron beam current is assumed to be 400 mA.

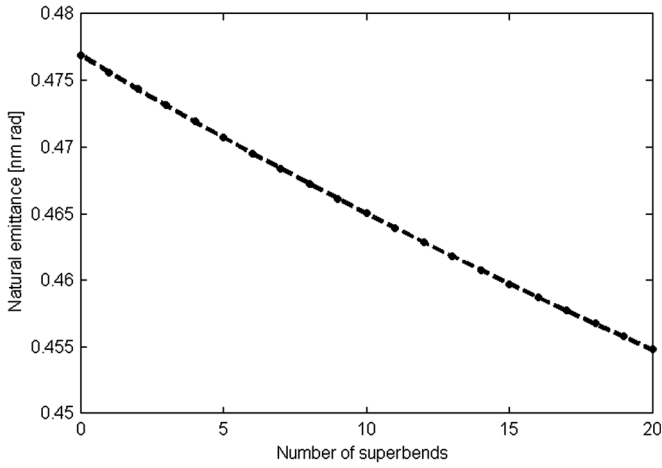


FIG. 3. Beam emittance reduction with the number of superbends in the storage ring.

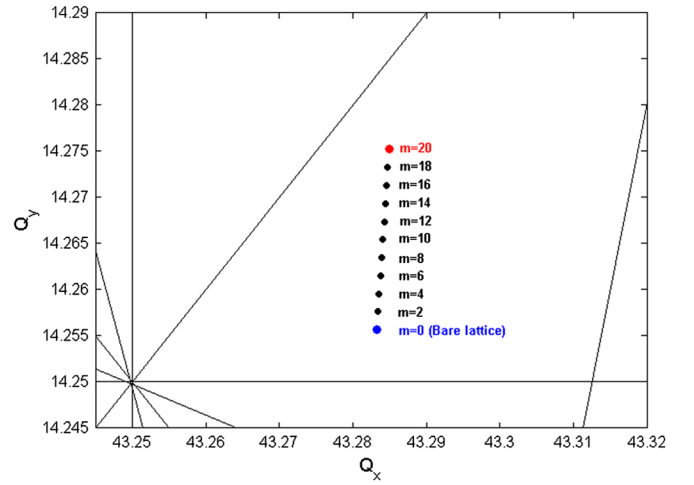


FIG. 4. Tune shift with the number of superbends in the storage ring lattice. Blue and red filled circles represent without and with 20 superbends in the lattice, respectively.

$$\varepsilon = A \cdot \left[\frac{2Nh_0^3 \left(\int_0^{L_0} (H_1 + H_2) ds \right) + (N-m)h_0^3 \int_0^{L_0} H_3 ds + 2mh_0^3 \int_0^{L_0} H_{LF} ds + mh_H^3 \int_0^{L_H} H_{HF} ds}{4Nh_0^2 L_0 + (N-m)h_0^2 L_0 + 2mh_0^2 \frac{L_0}{3} + mh_H^3 L_H} \right], \quad (1)$$

where A is a constant coefficient, N is the number of superperiods, m is the number of superbends, and L_0 and h_0 are the total length and the curvature of the low-field dipoles in the bare lattice, respectively. L_H is the length of the superbend high-field section, which is equal to 14.91 cm. The theoretically calculated beam emittance versus number of superbends is displayed in Fig. 3. It indicates that the beam emittance will reduce to about 0.455 nm rad with the use of the maximum number of superbends.

The shift of the tune point with the number of superbends is displayed in Fig. 4. It shows that the original tune point $Q_x = 43.283$, $Q_y = 14.255$ specified with blue color smoothly shifts to $Q_x = 43.285$, $Q_y = 14.275$ for the ILSF storage ring with 20 superbends. Low values of the tune spread, particularly Q_x , demonstrate a promising behavior of the new tune point even by using the highest number of superbends in the lattice. The main ILSF storage

ring parameters without and with 20 superbends are compared in Table I.

The high-field section of the superbend with a magnetic field of 1.4 T is located at the symmetry point of the bare lattice where the dispersion function is small. Therefore, the linear and nonlinear parameters of the lattice have been changed a little from their nominal values. The optical functions in a superperiod of the storage ring including the superbend are depicted in Fig. 5. For the new given tune point of the ILSF storage ring, the dynamic aperture of on-off momentum particles is evaluated by the numerical particle tracking. Figure 6 shows that the physical stable space is large enough to provide good beam injection efficiency and a long Touschek lifetime. It should be noted that the natural horizontal and vertical chromaticity is corrected close to a positive value (2.0 and 2.2) by the use of 16 sextupole magnets grouped in eight families. The shift of the tune point with energy deviation and the corresponding frequency map

TABLE I. Changes of the main ILSF storage ring parameters in the presence of 20 superbends.

Parameters	Units	Bare lattice	Bare lattice with 20 superbends
Energy (E)	GeV	3	3
Circumference (C)	m	528	528
Betatron tune (Q_x/Q_y)	.../...	43.283/14.255	43.285/14.275
Natural chromaticity (ξ_x/ξ_y)	.../...	-99.430/ - 52.830	-99.503/ - 52.676
Energy spread (δ)	...	7.028×10^{-4}	7.380×10^{-4}
Damping time ($\tau_x/\tau_y/\tau_s$)	ms/ms/ms	19.709/19.716/9.859	18.645/18.628//9.309
Energy loss (U)	keV	536	567
Momentum compaction (α_c)	...	1.523×10^{-4}	1.525×10^{-4}

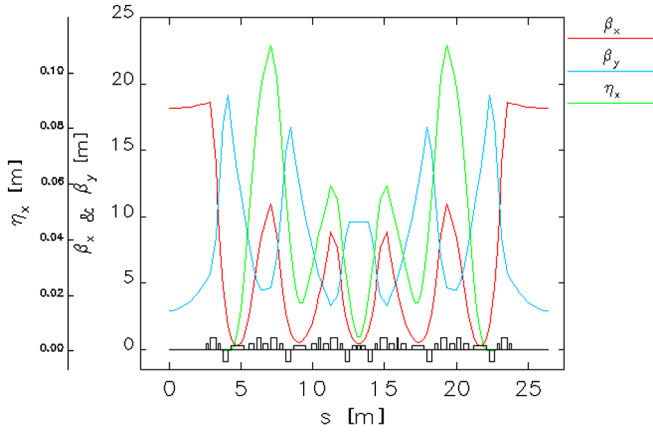


FIG. 5. The optical functions in a superperiod of the storage ring including a superbend in the middle of the lattice.

analysis of the storage ring are plotted in Figs. 7 and 8, respectively. The results indicate promising beam behavior as presented in Ref. [9] for the new tune point without any further optics optimizations.

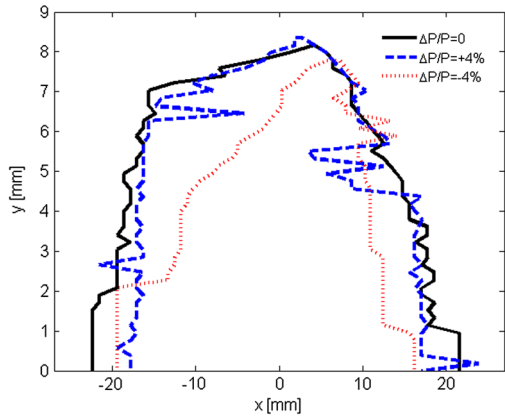


FIG. 6. Dynamic aperture at the center of the straight section. The particle tracking is performed 5000 turns through the storage ring with 20 superbends.

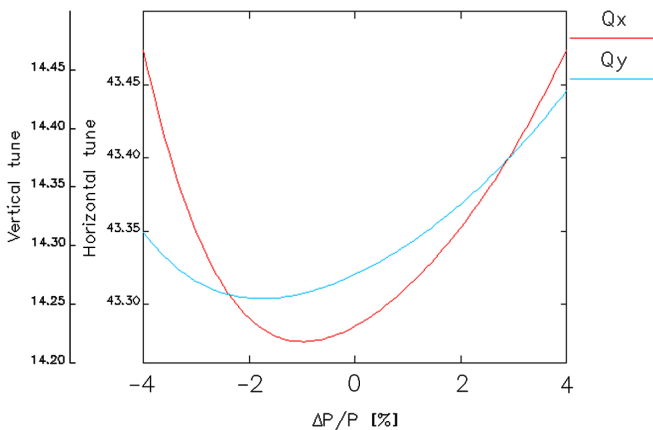


FIG. 7. Shift of the tune point with energy deviation. 20 superbends are included in the storage ring.

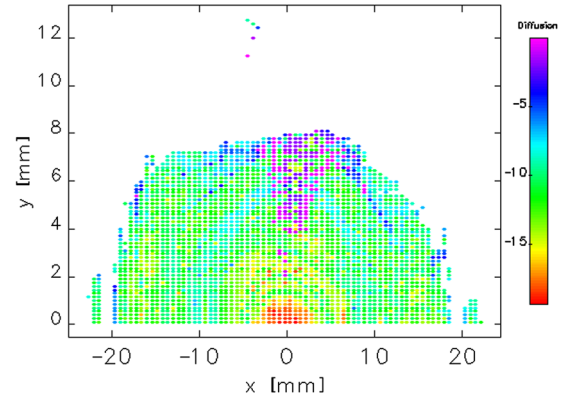


FIG. 8. Frequency map analysis of the storage ring with 20 superbends. The on energy electrons have been tracked 5000 turns through the storage ring. The colors indicate diffused transverse fractional tunes, $\log \sqrt{\Delta Q_x^2 + \Delta Q_y^2}$.

III. SUPERBEND ELECTROMAGNET DESIGN

The C-type ILSF dipole magnet is designed in a straight shape rather than curved form to simplify the fabrication procedure of the magnet core and coils [30]. The main dipole is divided in three straight sections, all with the same specifications. This is rather feasible, since the short bulk magnet yields a small sagittal, small pole width, and significant savings in the amount of iron core material. One shared hollow conductor coil is employed for the three sections; see Fig. 9. In the superbend, the middle low-field dipole section is replaced with a thin high-field dipole while the integrated field is kept constant. The high-field dipole section with an individual common coil specified

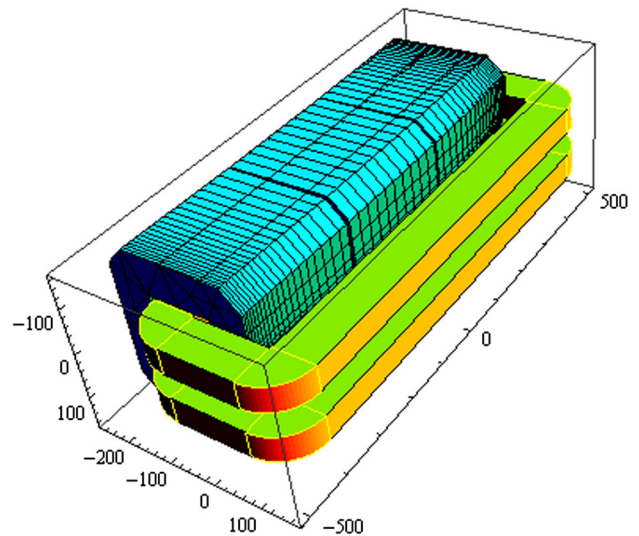


FIG. 9. 3D design of the main ILSF dipole magnet which is divided in three similar sections. Each dipole section has the length of 28 cm and bends the beam 1.2° . The angle between the middle section and lateral sections is 1.2° . The scale is millimeter.

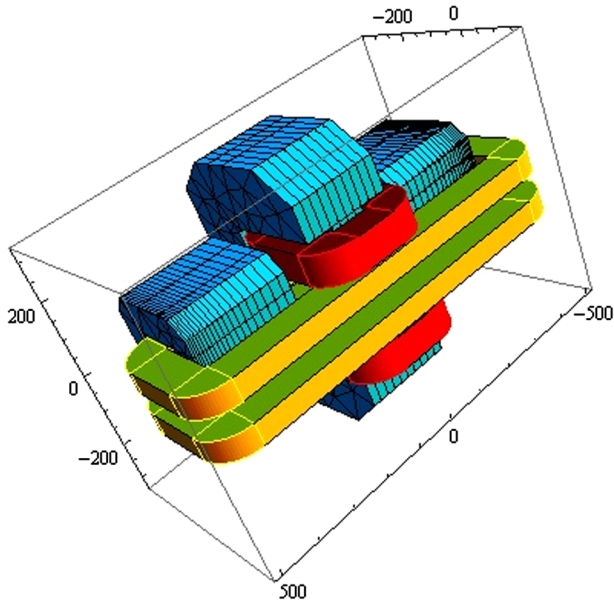


FIG. 10. 3D design of the superbend magnet. The high-field dipole section has the length of 14.91 cm and bends the beam 1.2° . The scale is millimeter.

with red color in Fig. 10 is flanked by the two low-field sections.

The locally available low carbon steel, ST14, with a standard number of 1.0338 is selected as the main material that results in significant fabrication cost reduction of the dipoles and the superbends. The measured B-H curve and relative permeability graph of ST14 are shown in Fig. 11. They indicate that the saturation field of the ST14 material is about 1.6 T where the relative permeability decreases to less than 500 [18–19].

A. 2D magnet design

The pole profile is the most important and complicated part of the magnet design. Magnetic field quality within the good field region (GFR) strongly depends on the pole

design. The required horizontal GFR in the superbend is ± 13.3 mm. The sagittal of its low-field and the high-field dipole sections is 0.73 mm and 0.39, respectively. Therefore, the total GFR of ± 14 mm is utilized as a design requirement of the superbend, and the field quality is considered to be less than 0.01% within the total GFR.

The gap of the superbend magnet has been determined mostly by the requirements of vacuum systems and beam dynamics issues. The thickness of the storage ring vacuum chamber is 2 mm, and an additional 2 mm is utilized as the clearance between the vacuum chamber and the magnet pole [31]. The required vertical GFR is ± 11 mm, which results in a half gap of 15 mm for the superbend. Moreover, the allowed relative higher order multipoles have been controlled by using the appropriate nonsymmetric standard shims. The main parameters utilized for the ILSF superbend magnet design are given in Table II, and the designed pole profile of both low-field and high-field dipole sections of the superbend in the presence of the vacuum chamber is shown schematically in Fig. 12. The corresponding 2D mechanical layouts are given in Fig. 13, which indicates total lamination dimensions of 300×330 and 420×650 mm² for the low-field and high-field dipole sections, respectively.

1. Magnetic field

The magnetic field and its quality inside half of the low-field and high-field yokes of the designed superbend are depicted in Figs. 14 and 15, respectively. They display the average quantity of the magnetic field in low- or high-field dipole section whose field quality is less than 1×10^{-4} or 7×10^{-5} within the GFR. The relative permeability shown in Fig. 16 indicates that both low-field and high-field dipole sections are far away from the saturation in the 2D design except sharp edges.

Moreover, the saturation tests were done by sketching the magnetic field versus current I . Figure 17 depicts that the operation currents of the low-field and high-field dipole

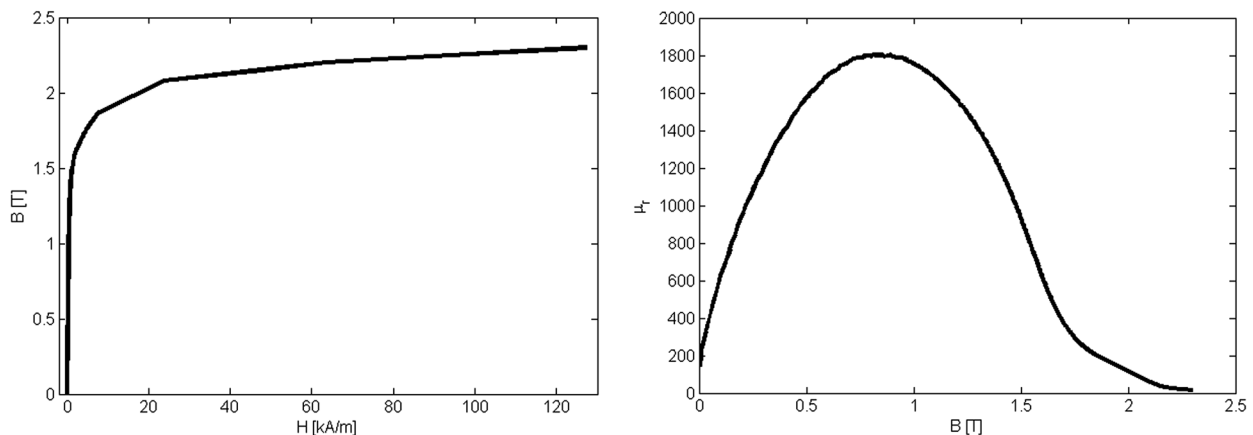


FIG. 11. (Left) The measured B-H curve and (right) relative permeability of ST14.

TABLE II. Main parameters utilized for the ILSF superbend magnet design.

	Length (mm)	Dipole field (T)	Total horizontal GFR (mm)	Gap height (mm)
High-field section	149.1	1.405	± 14	30
Low-field section	280	0.748	± 14	30

sections are 382 and 694 A (382 A for the shared coil and 312 A for the individual coil), and their deviations from the corresponding linear curves are less than 0.4% and 0.6%, respectively.

2. Harmonic analysis

The higher order multipole components due to the finite pole profile and the saturation of the material significantly affect the dynamic aperture. The assumed magnetic field expansion at midplane ($y = 0$) is

$$B_y(x) = \sum_{n=1}^{n=\infty} B_n = \sum_{n=1}^{n=\infty} b_n x^{n-1}, \quad (2)$$

where n is the order of multipole component and b_n is the multipole coefficient. Systematic multipole components obtained with the POISSON [21] code are given in Table III, and the normalized multipole errors are depicted in Fig. 18.

3. Static mechanical analysis

There is a yoke deflection when the electromagnet is powered on [32]. This deflection is caused by the magnetic force between the poles. The pole deflection in the presence of such a force and weight of the laminations is evaluated for the designed superbend, and the results are displayed in Fig. 19. As shown, the maximum pole deflection in the low-field and high-field dipole sections is less than 0.04 and 0.05 mm, respectively. The deflected pole produces quadrupole gradients of 0.57 and 0.70 Gauss/cm. The field quality increases to 1.4×10^{-4} (9.2×10^{-5}) in low- (high-)

field dipole section. However, one can overcome these undesired gradients and pole deflection by fine adjustment of the quadrupoles in the lattice and increasing the width of the return yoke or welding a plate to it [33].

B. 3D magnet design

The ends of the magnet cores should be designed in such a way that could provide the desired magnetic length and to avoid saturation and dangerous higher order multipoles. For these proposals, the end poles of the lattice central dipole are chamfered at first in the design process. The middle section of the central dipole is then replaced with a thin high-field section. To keep the same integrated field with acceptable quality, the end poles of the inserted high-field dipole section are chamfered next.

1. Lattice central dipole chamfering

In order to design the lattice's central low-field dipole in 3D, one straight block model with identical geometry to the current engineering layout (Fig. 9) is designed instead of three dipole sections. This should not affect the validity of the data predicted by the simulation, but it simplifies the 3D modeling. The magnetic length will be achieved by using chamfers at the pole ends. The chamfering will additionally control higher integrated multipoles. The chamfered pole end of the lattice central dipole is drawn in Fig. 20. The end pole profile and its roll-off follow the Rogowski curve [34]. The chamfering angle from the pole edge is 52° .

The magnetic field homogeneity in the transverse plane ($s = 0$) is examined, and the resulting field quality, not shown here, was as good as the corresponding 2D calculation which demonstrates that the three- and two-dimensional models are consistent. The integrated field quality with and without chamfering is plotted in Fig. 21, which indicates that the optimized chamfer improves it from 6×10^{-4} to 1.5×10^{-4} within the total good field region.

To estimate the magnetic length, the vertical field generated by the roll-off was integrated longitudinally through the magnet:

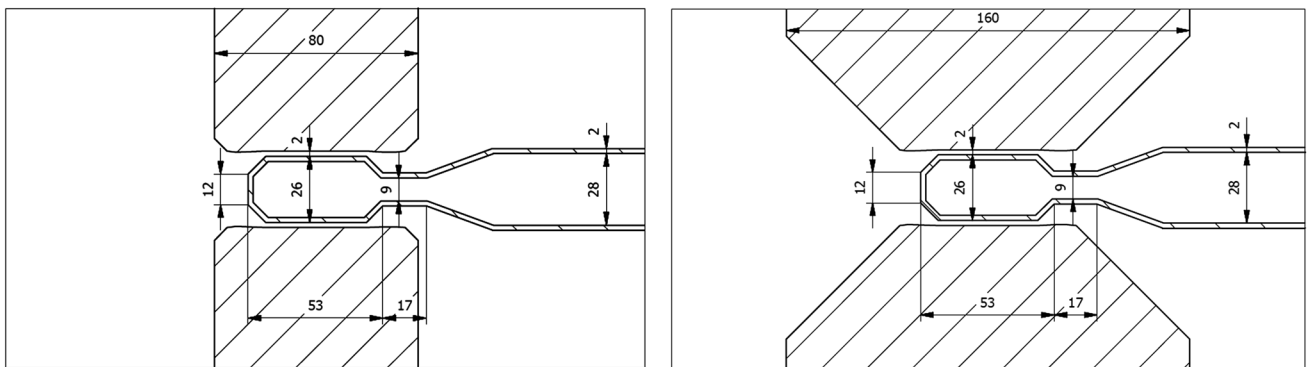


FIG. 12. Pole profile of the designed (left) low-field and (right) high-field dipole sections in the presence of the vacuum tube [15]. The scale is millimeter.

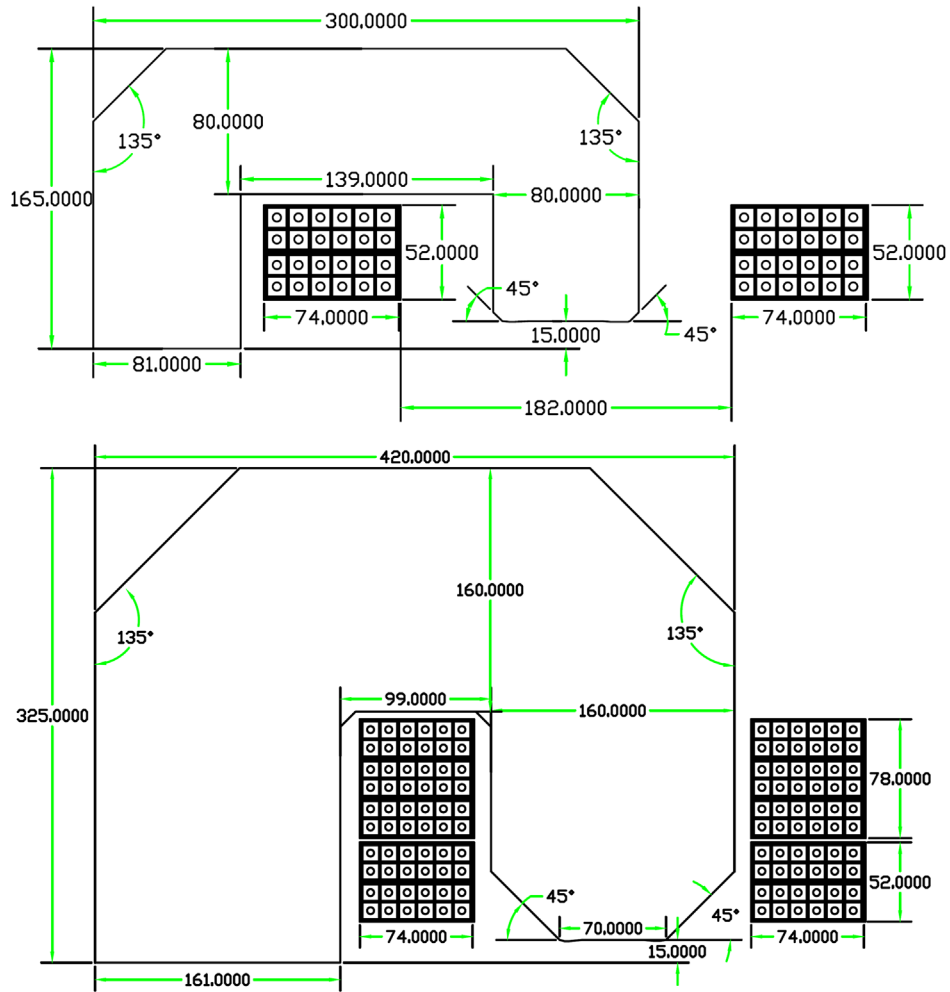


FIG. 13. Laminations' and coils' dimensions of the (top) low-field and (bottom) high-field dipole sections of the superbend. The scale is millimeter.

$$L_{\text{eff}} = \frac{\int B ds}{B_{\text{center}}} \tag{3}$$

The calculated effective length of the lattice central dipole at the center ($x = 0$) is 839.5 mm, which is 0.5 mm less than the desired magnetic length. These results

will be further examined prior to proceeding with the procurement exercise for the dipole, and, if necessary, small adjustments will be made to the end roll-off to provide the required magnetic length of 840 mm. The maximum effective length deviation within the GFR of ± 14 mm is

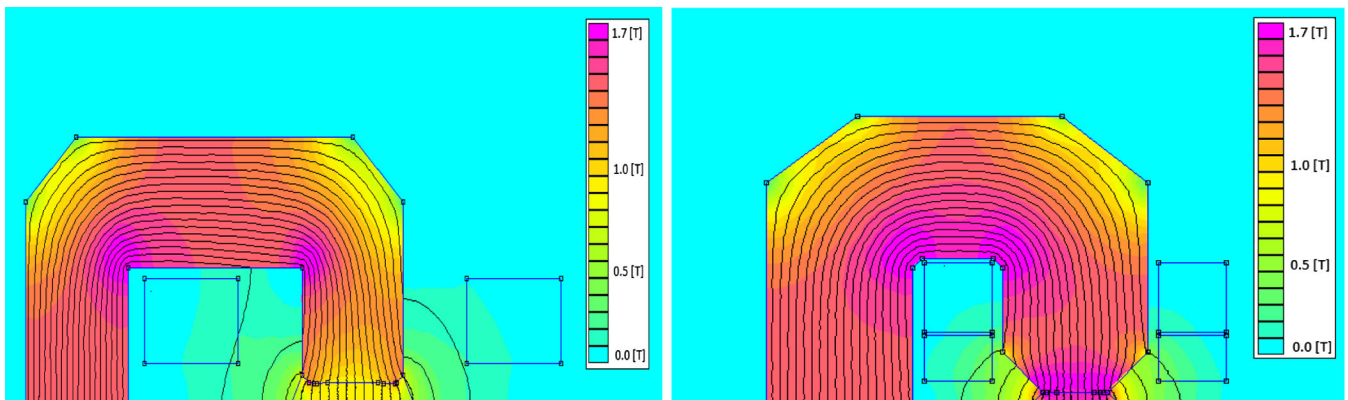


FIG. 14. Magnetic field inside half of 2D designed (left) low-field and (right) high-field dipole sections of the superbend.

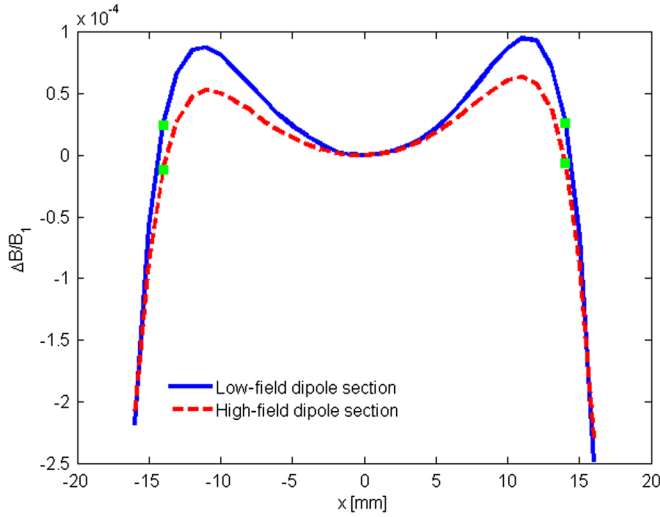


FIG. 15. Field quality of 2D designed low-field and high-field dipole sections of the superbend. The green filled rectangles represent ± 14 mm GFR.

less than 0.15 mm. The field distribution along the half magnet length is shown in Fig. 22. It should be noted that the iron length of 820 mm is utilized in the calculations.

The higher order integrated multipoles at the $y = 0$ plane are given by

$$\frac{\int B_y(\varphi, s) ds}{L} = \sum_{n=1}^{\infty} A_n \cos((n-1)\varphi), \quad (4)$$

where the field coefficient A_n is

$$A_n = a_n \frac{r^{n-1}}{(n-1)!}$$

and a_n is the multipole coefficient. The higher integrated multipoles are given in Table IV, and their corresponding normalized values are depicted Fig. 23. As given, the relative integrated sextupole component is less than 10^{-4} ,

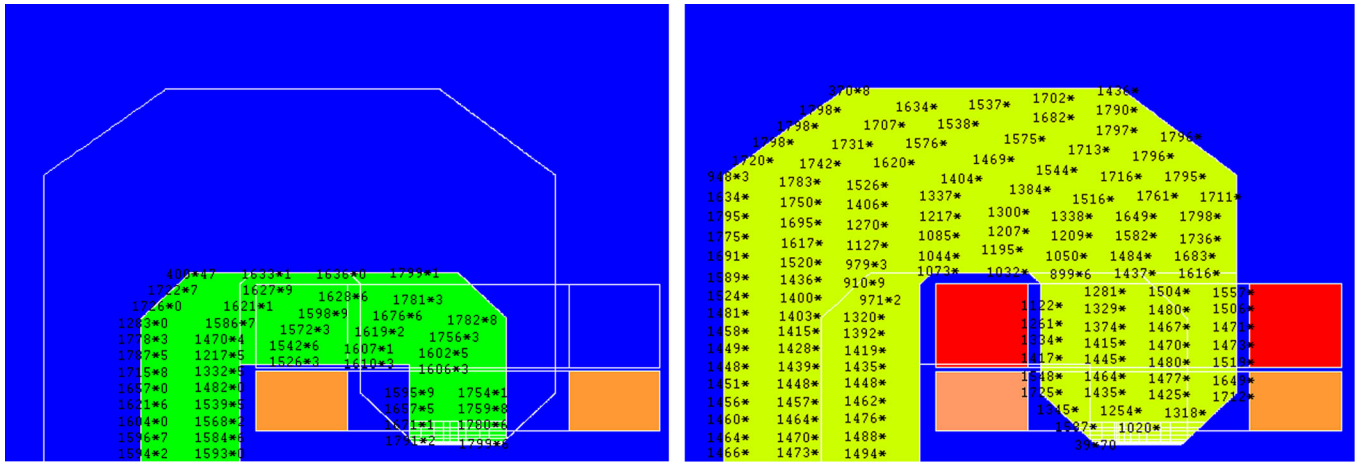


FIG. 16. Relative permeability in half of 2D designed (left) low-field and (right) high dipole sections of the superbend.

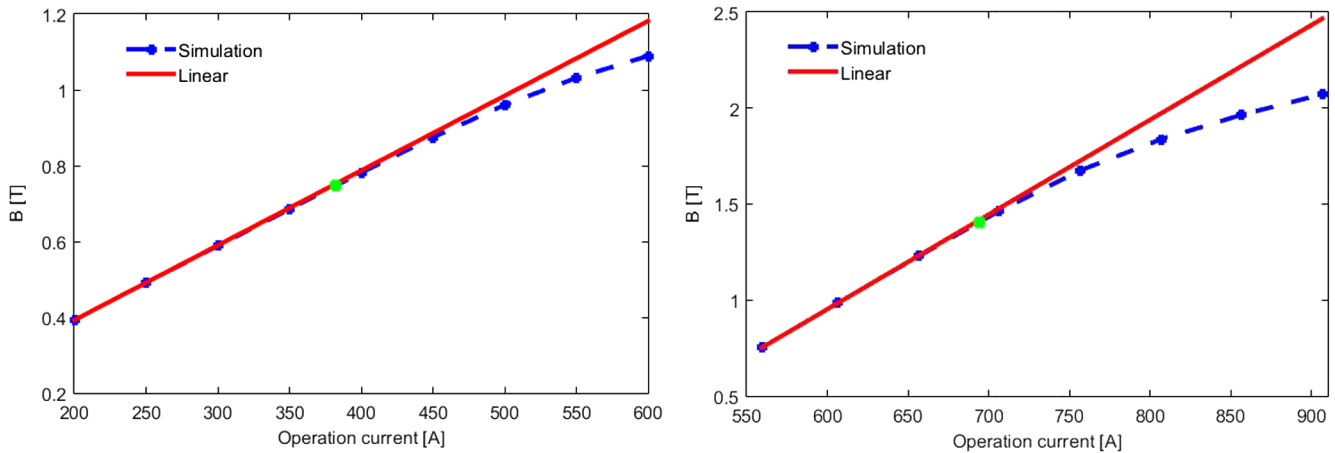


FIG. 17. The magnetic field as a function of the operation current of the designed (left) low-field and (right) high-field dipole sections. The green filled rectangles indicate the operation currents.

TABLE III. The systematic multipole components of 2D designed dipoles.

n	Low-field dipole section		High-field dipole section	
	B_n (T) @ 14 mm	b_n	B_n (T) @ 14 mm	b_n
1	-7.48×10^{-1}	-7.480×10^{-1}	-1.4055	-1.406
3	-1.33×10^{-4}	-6.763×10^{-1}	-0.00017	-8.690×10^{-1}
5	-4.19×10^{-5}	-1.092×10^3	-5.4×10^{-5}	-1.406×10^3
7	7.56×10^{-5}	1.004×10^7	0.000123	1.631×10^7
9	5.90×10^{-5}	3.995×10^{10}	9.25×10^{-5}	6.265×10^{10}
11	2.18×10^{-5}	7.536×10^{13}	2.84×10^{-5}	9.819×10^{13}
13	1.18×10^{-5}	2.075×10^{17}	7.11×10^{-6}	1.255×10^{17}
15	1.80×10^{-5}	1.616×10^{21}	9.62×10^{-6}	8.653×10^{20}

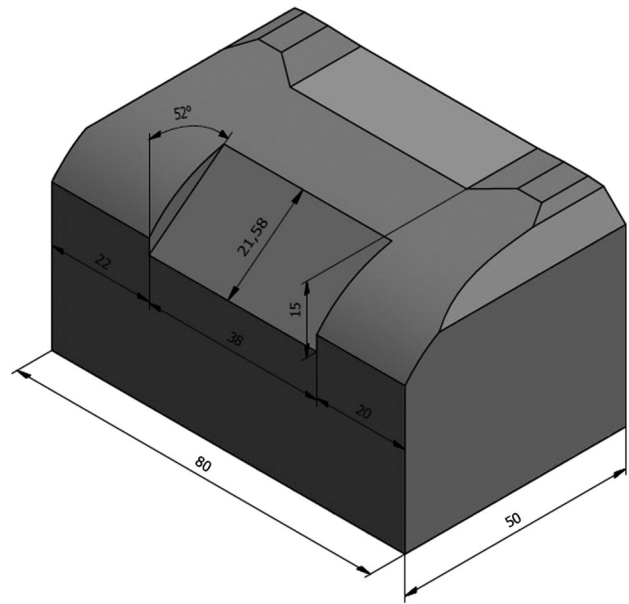


FIG. 20. Mechanical design of the chamfered one end pole of the lattice main dipole. The scale is millimeter.

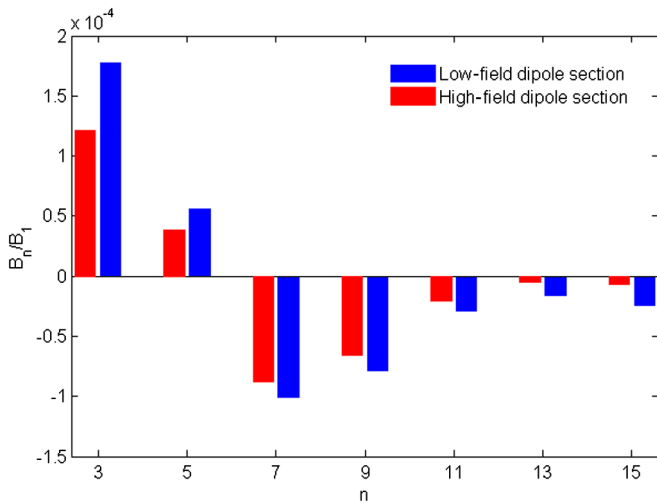


FIG. 18. The normalized systematic multipole field errors of 2D designed low-field and high-field dipole sections at the GFR of 14 mm.

which indicates an expected small impact on the dynamic aperture.

2. Superbend magnet

To keep the integrated field of the superbend the same as the lattice central dipole, the length and chamfer of the high-field dipole section should be optimized. The high-field dipole section is modeled in three dimensions based on the nonlinear finite element method. The 3D modeling shows that the optimal thickness of the high-field magnet pole should be 92 mm, which results in the

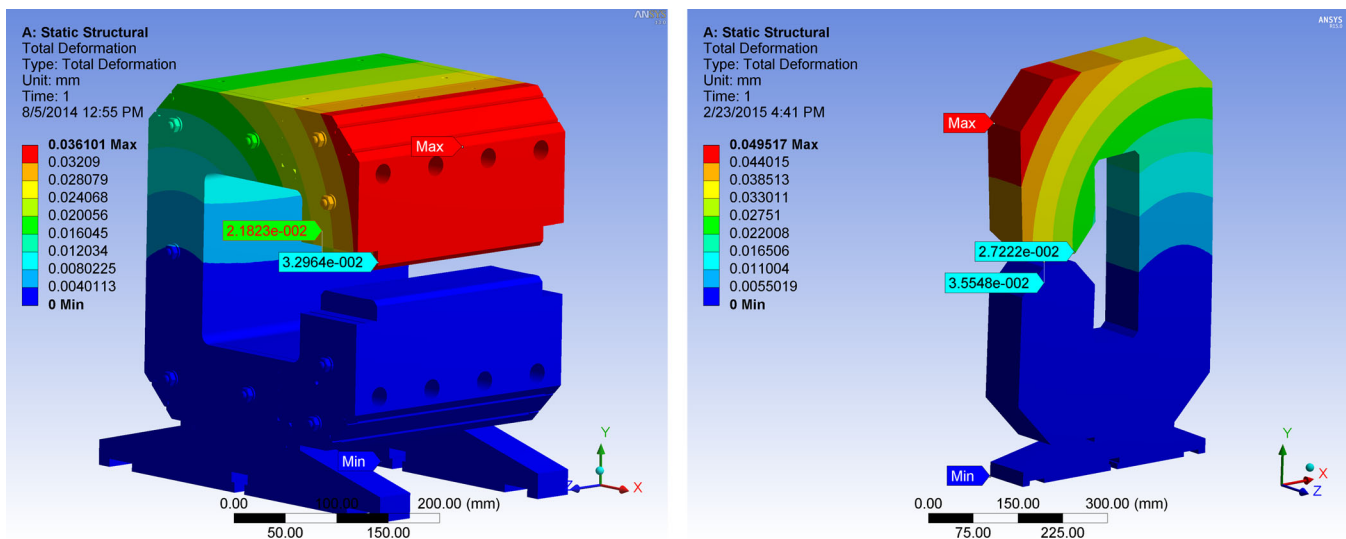


FIG. 19. Static mechanical analysis for the (left) low-field and (right) high-field dipole sections of the superbend.

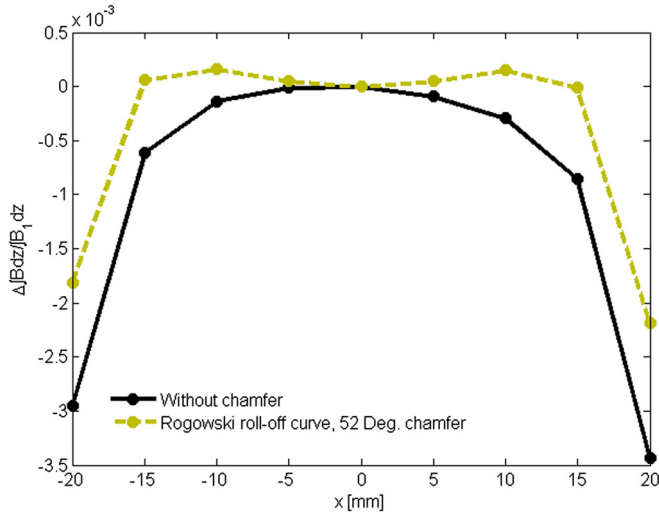


FIG. 21. Integrated field quality of the main dipole magnet in the $y = 0$ plane with and without a chamfer.

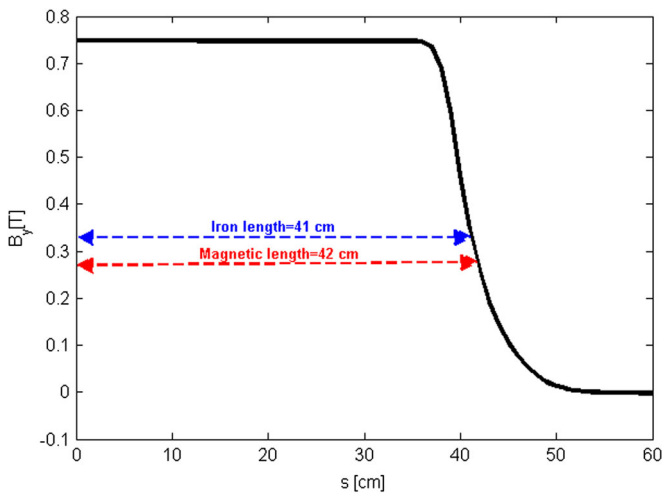


FIG. 22. Variation of the vertical field of half the main dipole along the longitudinal direction.

desired magnetic field of 1.4 T. In order to avoid extra saturations, the thickness of the return core outside the coil is increased to the optimum value of 211 mm; see Fig. 24.

TABLE IV. The integrated multipole field coefficients [22].

n	a_n	A_n (kGs) @ (14 mm)
1	5.234	5.234
3	-0.00026	-0.00025
5	0.00900	0.00144
7	-0.18051	-0.00188
9	0.26351	0.00009
11	9.26298	0.00007
13	-4.80×10^3	-0.00056
15	5.97×10^5	0.00076
17	-6.9×10^7	-0.00071

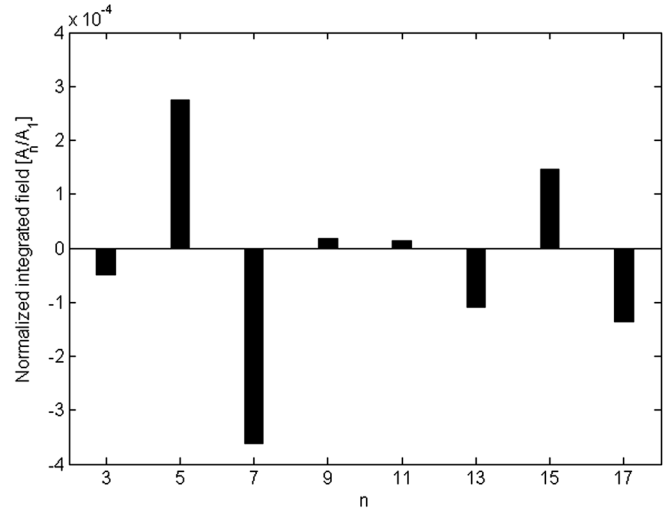


FIG. 23. Normalized integrated field at a horizontal distance of 14 mm.

The 3D calculated relative permeability in the high-field section of the superbend magnet is shown in Fig. 25, which differs from its 2D calculation because of its pole saturation. It is unavoidable and we have to live with it. However, no saturation is seen in the return yoke because of its larger thickness. The field in the gap distribution within half of the superbend magnet (with both high-field and low-field sections considered simultaneously, Fig. 10) is depicted in Fig. 26.

The field qualities of the low-field and high-field dipole sections in the horizontal direction are shown in Fig. 27. The 3D simulations show that the field quality in the

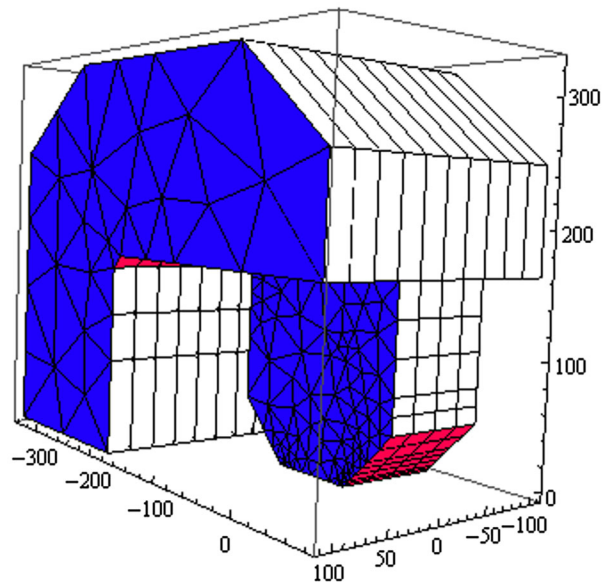


FIG. 24. 3D design overview of the half yoke of the high-field dipole section. The thickness of the return core is increased to avoid saturation. The scale is millimeter.

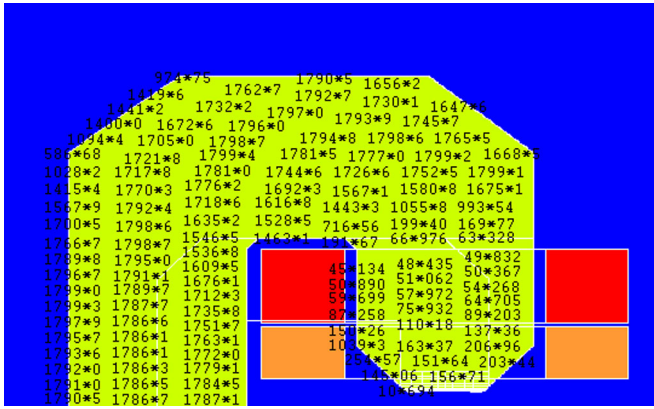


FIG. 25. The relative permeability in the 3D design of the high-field dipole section (at $s = 0$).

low-field section is similar to 2D calculations and is less than 1×10^{-4} . However, due to the saturation in the inserted thin high-field section, the field quality is increased from 1×10^{-4} in 2D to 2×10^{-4} in 3D.

In order to provide good integrated field quality along the superbend, both pole ends of the high-field section are chamfered by 26° . As compared in Fig. 28, the integrated field quality is improved from 1.5×10^{-3} to 1.5×10^{-4} within the total GFR.

C. Mechanical design

The designed ILSF dipole magnet is composed of three straight yokes placed on one girder. The mechanical angle between the middle yoke and side ones is 1.2° . The shared long hollow conductor coils are mounted around all the yokes. The mechanical 3D model is shown in Fig. 29 (left). Each straight yoke is based on the stacked C-type

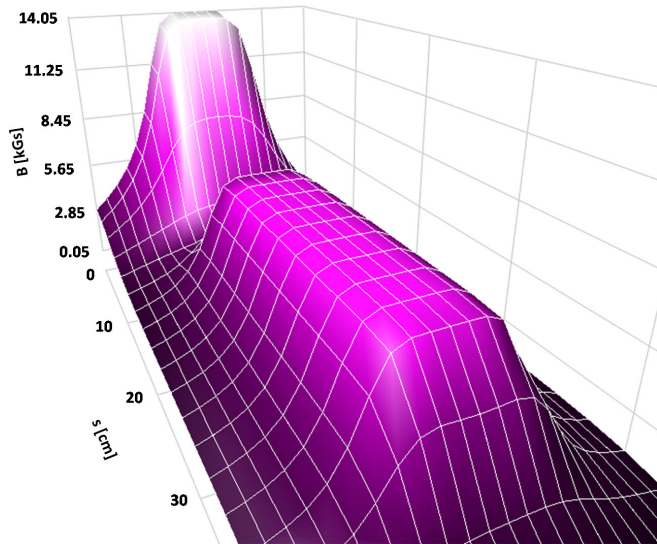


FIG. 26. Gap field variation along half of the superbend. The chosen fields for the low-field and high-field dipole sections are 0.75 and 1.41 T, respectively.

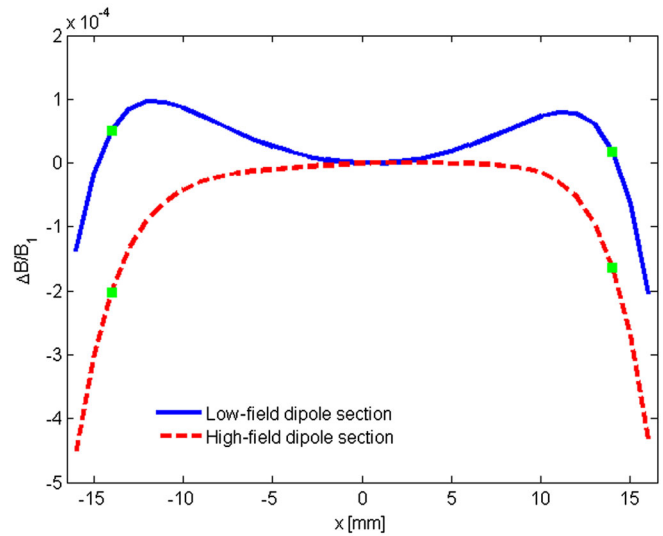


FIG. 27. The field quality in low-field and high-field dipole sections of the superbend in the 3D design. The green filled rectangles represent ± 14 mm GFR.

laminations. The laminations with a thickness of 1 mm are stacked with the packing factor of 98% by the local epoxy resin of EL-413, with a hardener of HA-41, which is similar to the epoxy resin of Araldite F, with a hardener of ARADVR HY 905. Additionally, several tension plates are also welded at different parts of the yokes to avoid tilting and separating the laminations. The magnet gap opening to the radial inwards part of the ring allows installation of the vacuum chamber. The middle laminated yoke consists of a block bottom and a block top half assembled together, which allows replacing the middle yoke with a high-field section. The top and bottom halves of the high-field sections mounted with additional individual common coils

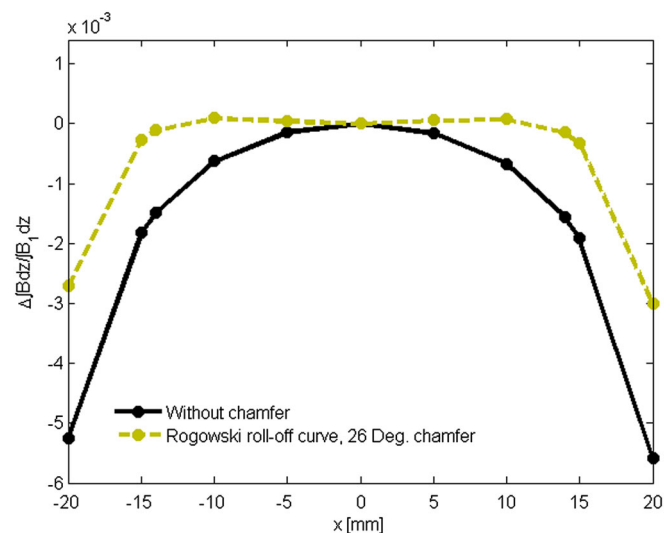


FIG. 28. The integrated field quality of the superbend magnet with and without a chamfer on the high-field section.

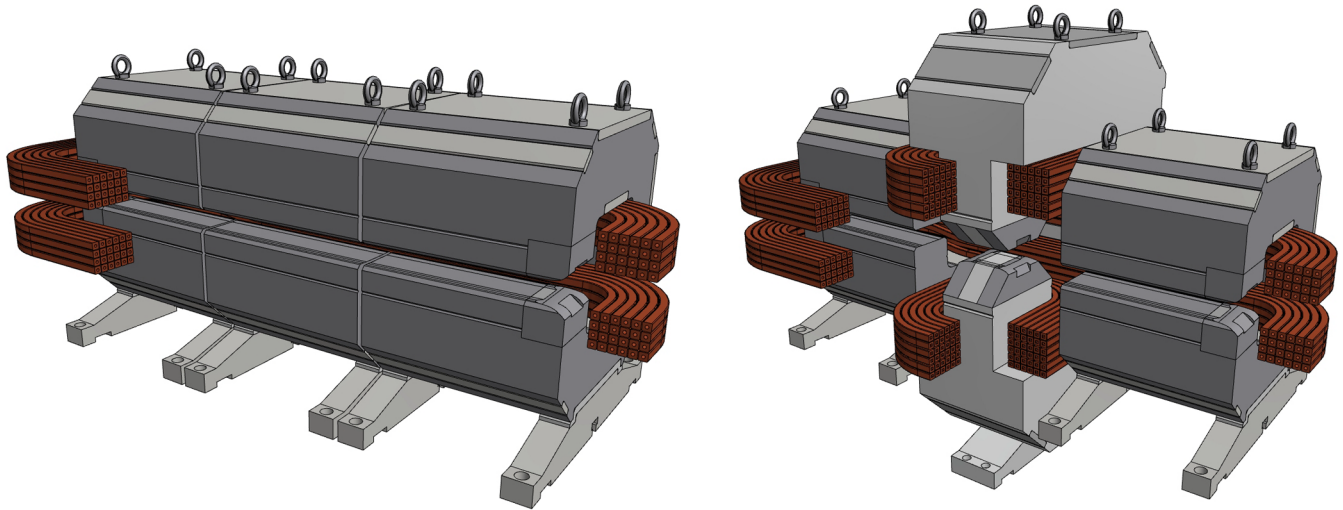


FIG. 29. Perspective mechanical design of the (left) lattice central low-field dipole and (right) superbend magnet [15].

are assembled together instead of the middle low-field yoke [Fig. 29 (right)].

D. Electrical and cooling calculations

For electrical and cooling calculations, conductor and cooling duct dimensions should be chosen to provide optimum current density, power, inductance, cooling water speed, and pressure drop. There are two coils in the superbend magnet: one shared coil for all the sections and one individual only for the inserted high-field section. The water flow velocity should be high enough so that the flow is fully turbulent with a Reynolds number ≥ 4000 . On the other hand, an acceptable water speed to avoid vibration and erosion of the conductor must be less than 4 m/s [32]. Furthermore, regarding local availability, 11×11 mm² of the oxygen-free copper conductor duct with a cooling hole of 4.5 mm diameter has been selected; see Fig. 30. It is worth mentioning that glass fiber insulation treated with silicone varnish for adhesion and impregnation with 0.5 mm thickness would be implemented for both shared and individual coils. The calculated electrical and cooling

parameters of the superbend are given in Table V. Because of the use of one cooling system for the superbend, the same pressure drops are considered for both coils in the calculations.

TABLE V. The superbend electrical and cooling specifications.

Parameter	Shared coil of the superbend	Individual coil of the high-field section
Total amp-turns per coil (A.T)	9168	11235
Operating current (A)	382	312
Number of turns per coil	24	36
Number of pancakes per coil	2	3
Conductor dimensions (mm)	11 × 11	11 × 11
Water cooling tube diameter (mm)	4.5	4.5
Copper area (mm ²)	105	105
Current density (A/mm ²)	3.64	3
Resistance per magnet (mΩ)	23	16.4
Voltage drop per magnet (V)	8.81	5.13
Power per magnet (KW)	3.37	1.60
Number of water circuits	4 (each coil has 2)	2 (each coil has 1)
Pressure drop (bar)	6.0	6.0
Water temperature rise (°C)	5.63	6.54
Cooling water speed (m/s)	2.25	1.84
Reynolds number	5060	4130

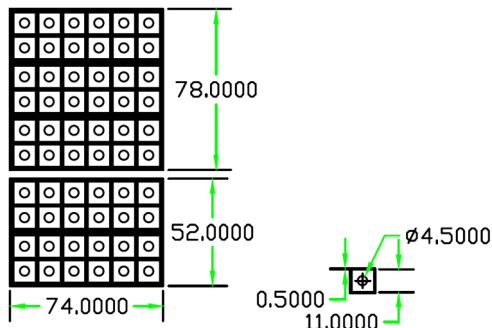


FIG. 30. Cross section of the selected hollow conductor coils.

IV. CONCLUSIONS AND OUTLOOK

The ILSF storage ring is based on the five-bend achromat lattice with the circumference of 528 m, which provides the beam emittance of 0.48 nm rad. In order to produce very bright high energy radiation, a superbend solution is chosen for use instead of the lattice central low-field dipole. The longitudinal step function field gradient of the superbend reduces the beam emittance desired by the users. The impacts of employing the superbend on the ILSF storage ring main parameters and the related beam dynamics have been discussed. The results revealed that the linear and nonlinear parameters of the lattice have been slightly changed from their nominal values and indicate promising beam behavior even without any further optimizations. The design of the superbend magnet with common coils has been physically and mechanically described. The proper end chamfers for the low-field and high-field dipole sections are developed and fully determined to meet the integrated field uniformity requirement. The designed superbend is now ready for fabrication as a prototype for the ILSF.

ACKNOWLEDGMENTS

The authors especially thank H. Wiedemann for his many helpful comments on this research. We are grateful to Y. Pupkov for his kind advice. We also appreciate ILSF Mechanic group which provided mechanical drawings for this paper. This work is fully supported by the Iranian Light Source Facility.

-
- [1] J. Rahighi, in *Proceedings of the International Particle Accelerator Conference, Kyoto, Japan* (ICR, Kyoto, 2010), pp. 2532–2534; <http://ilsf.ipm.ac.ir/>.
- [2] J. Rahighi *et al.*, in *Proceedings of the 2nd International Particle Accelerator Conference, San Sebastián, Spain* (EPS-AG, Spain, 2011), pp. 2954–2956.
- [3] Y. Papaphilippou, A. Ropert, P. Elleaume, and L. Farvacque, in *Proceedings of the 21st Particle Accelerator Conference, Knoxville, TN, 2005* (IEEE, Piscataway, NJ, 2005), pp. 2047–2049.
- [4] S. Ozaki, J. Bengtsson, S. L. Kramer, S. Krinsky, and V. N. Litvinenko, in *Proceedings of the 22nd Particle Accelerator Conference, PAC-2007, Albuquerque, NM* (IEEE, New York, 2007), pp. 77–79.
- [5] M. Borland, G. Decker, L. Emery, V. Sajaev, Y. Sun, and A. Xiao, Lattice design challenges for fourth-generation storage-ring light sources, *J. Synchrotron Radiat.* **21**, 912 (2014).
- [6] P. F. Tavares, S. C. Leemann, M. Sjöström, and Å. Andersson, The MAX IV storage ring project, *J. Synchrotron Radiat.* **21**, 862 (2014).
- [7] J.-L. Revol *et al.*, in *Proceedings of the 4th International Particle Accelerator Conference, IPAC-2013, Shanghai, China, 2013* (JACoW, Shanghai, China, 2013), pp. 82–84.
- [8] L. Liu, N. Milas, A. H. C. Mukai, X. R. Resende, and F. H. de Sá, The Sirius project, *J. Synchrotron Radiat.* **21**, 904 (2014).
- [9] H. Ghasem, E. Ahmadi, F. Saeidi, and K. Sarhadi, Beam dynamics of a new low emittance third generation synchrotron light source facility, *Phys. Rev. ST Accel. Beams* **18**, 030710 (2015).
- [10] D. Robin *et al.*, Superbend upgrade on the Advanced Light Source, *Nucl. Instrum. Methods Phys. Res., Sect. A* **538**, 65 (2005).
- [11] J. Guo and T. Raubenheimer, in *Proceedings of the 8th European Particle Accelerator Conference, Paris, 2002* (EPS-IGA and CERN, Geneva, 2002), pp. 1136–1138.
- [12] R. Nagaoka and A. Wrulich, Emittance minimization with longitudinal dipole field variation, *Nucl. Instrum. Methods Phys. Res., Sect. A* **575**, 292 (2007).
- [13] Y. Papaphilippou and P. Elleaume, in *Proceedings of the 21st Particle Accelerator Conference, Knoxville, TN, 2005* (IEEE, Piscataway, NJ, 2005), pp. 2086–2088.
- [14] A. Streun and A. Wrulich, Compact low emittance light sources based on longitudinal gradient bending magnets, *Nucl. Instrum. Methods Phys. Res., Sect. A* **770**, 98 (2015).
- [15] J. Dehghani *et al.*, ILSF mechanics internal report, 2014.
- [16] James Citadini *et al.*, Sirius - A 3 GeV electron storage ring based on permanent magnets, *IEEE Trans. Appl. Supercond.* **22**, 4004404 (2012).
- [17] Tian Shun-Qiang *et al.*, Lattice design and optimization of the SSRF storage ring with super-bends, *Nucl. Sci. Techniques* **25**, 010102 (2014).
- [18] A. Shahveh *et al.*, ILSF magnet internal report No. ILSF-MG-TN-RE17-00-20140501, 2014.
- [19] A. Shahveh *et al.*, ILSF magnet internal report No. ILSF-MG-TN-RE07-01-20130701, 2013.
- [20] Finite Element Method Magnetics (FEMM), www.FEMM.info.
- [21] POISSON/SUPERFISH group of codes, Los Alamos National Laboratory Report No. LA-UR-87-126, 1987.
- [22] MERMAID code, SIM Limited, Novosibirsk department, 630058 Novosibirsk, P. O. Box 160, Russia.
- [23] RADIA magnet design code, <http://ftp.esrf.eu/pub/InsertionDevices/>.
- [24] A. Streun, OPA lattice design code, <https://ados.web.psi.ch/opa/>.
- [25] M. Borland, Advanced Photon Source, Argonne National Laboratory Report No. LS-287, 2000.
- [26] T. Tanaka and H. Kitamura, SPECTRA: A synchrotron radiation calculation code, *J. Synchrotron Radiat.* **8**, 1221 (2001).
- [27] Alexander Gabard *et al.*, in *Proceedings of the 2nd International Particle Accelerator Conference, San Sebastián, Spain* (EPS-AG, Spain, 2011), pp. 3038–3040.
- [28] R. Nagaoka *et al.*, in *Proceedings of the 3rd International Particle Accelerator Conference, New Orleans, LA, 2012* (IEEE, Piscataway, NJ, 2012), pp. 1155–1157.
- [29] R. P. Walker *et al.*, in *Proceedings of the 2nd International Particle Accelerator Conference, San Sebastián, Spain* (EPS-AG, Spain, 2011), pp. 3059–3061.

-
- [30] H. Tarawneh, L.-J. Lindgren, and B. Anderberg, Prototype soft end dipole magnet for MAX-IV, fabrication and measurements, *Nucl. Instrum. Methods Phys. Res., Sect. A* **546**, 620 (2005).
- [31] O. Seify, Vacuum group internal report No. ILSF-B-VG-SR00-DES-02-00I, 2014.
- [32] J. Tanabe, *Iron Dominated Electromagnets Design, Fabrication, Assembly and Measurements* (World Scientific, Singapore, 2005).
- [33] H. Wiedemann (private communications).
- [34] DIAMOND Light Source detailed design report, June, 2002.